Journal of Materials Chemistry C

ROYAL SOCIETY OF CHEMISTRY

PAPER

View Article Online
View Journal | View Issue

Cite this: J. Mater. Chem. C, 2024, 12, 19506

Enhanced oxygen electrode performance in solid oxide fuel cells *via* La-doping of $Pr_2NiO_{4+\delta}$-based Ruddlesden–Popper perovskites†

Zihao Liao,[a] Yiping Yang,[a] Dingrong Ou,[a] Yuan Tang,[a] Bo Wang,[a] Binbin He,[a] Yu Zeng,[b] Yunfeng Tian *[c] and Bo Chi [b]

Received 30th August 2024,
Accepted 21st October 2024

DOI: 10.1039/d4tc03740e

rsc.li/materials-c

Solid oxide fuel cell (SOFC) is a high-efficiency, low-carbon power generation device that directly converts the chemical energy of fuel directly into electricity at elevated temperatures. However, the performance of the oxygen electrode, which is critical for the oxygen reduction reaction (ORR), remains limited by high polarization losses and limited long-term stability. Ruddlesden–Popper (R–P) perovskites, such as $Ln_2NiO_{4+\delta}$ (Ln = La, Pr, Nd), offer excellent oxygen transport due to their unique A–O rock salt layers. In this study, La^{3+}-doped $Pr_{2-x}La_xNi_{0.8}Cu_{0.2}O_{4+\delta}$ (x = 0, 0.5, 1.0, PL_xNC) oxygen electrode materials are synthesized by the sol–gel method, and their electrochemical properties are systematically investigated. While the electrical conductivity decreases with increasing La^{3+} content, $PL_{0.5}NC$ exhibits optimal oxygen surface exchange and bulk diffusion properties. SOFC using $PL_{0.5}NC$ as the oxygen electrode achieved excellent performance at 800 °C, with a polarization resistance of 0.245 Ω cm^2 and a peak power density of 0.864 W cm^{-2}, a 64% improvement over PNC. This study highlights the potential of La^{3+} doping to enhance PNO-based oxygen electrodes and provides insight into the development of high performance SOFC materials.

1. Introduction

Solid oxide fuel cells (SOFC) efficiently convert chemical energy into electrical energy using hydrocarbon fuels such as H_2, CH_4, and CH_3OH to generate electricity.[1,2] The oxygen electrode, a key component in SOFC, drives the oxygen reduction reaction (ORR).[3] Ideal oxygen electrode materials require high thermodynamic stability, mixed ionic–electronic conductivity, enhanced catalytic activity, and adequate porosity.[4] Currently, conventional ABO_3-type perovskite oxides, such as $LaMnO_3$-based compounds (LSM),[5,6] $La_{1-x}Sr_xCo_{1-y}Fe_yO_3$ (LSCF),[7,8] and $Ba_{1-x}Sr_xCo_{1-y}Fe_yO_3$ (BSCF),[9,10] are commonly used as oxygen electrodes. However, the low oxygen ion conductivity of LSM limits its ORR efficiency, while the long-term stability of LSCF and BSCF is compromised by the presence of alkaline earth metals such as Ba and Sr.[11] Therefore, the development of new oxygen electrode materials with enhanced performance and stability remains a pressing challenge.

Ruddlesden–Popper (R–P) perovskites, represented by the formula $Ln_2NiO_{4+\delta}$ (Ln = La, Pr, Nd), are a remarkable class of mixed ionic electronic conductors (MIECs) with the general structural formula $A_{n+1}B_nO_{3n+1}$ or $AO(ABO_3)_n$. Unlike conventional perovskites, R–P perovskites have a distinctive layered structure in which A–O layers alternate with rock salt and ABO_3 perovskite layers along the c-axis. This unique A–O layer can accommodate excess interstitial oxygen, thereby enhancing oxygen ion conductivity. R–P perovskites are characterized by high oxygen ion diffusion coefficients and surface exchange rates, making them promising candidates for oxygen electrode materials.[12–14] These materials have demonstrated favorable electrocatalytic activity for the ORR. For example, the $La_{1.5}Pr_{0.5}Ni_{0.8}Co_{0.2}O_{4+\delta}$ oxygen electrode achieved a peak power density of 0.4 W cm^{-2} at 700 °C in fuel electrode-supported SOFCs.[15] Similarly, $Pr_2NiO_{4+\delta}$ electrodes exhibited a peak power density of 0.95 W cm^{-2} at 750 °C, with a degradation rate of less than 3%/1000 h at a constant voltage of 0.8 V.[16] Among the $Ln_2NiO_{4+\delta}$ series, $Pr_2NiO_{4+\delta}$ (PNO) stands out for its exceptional oxygen surface exchange (k^*) and bulk diffusion (D^*) coefficients, recorded at 2.5 cm s^{-1} and 5.0 × 10^{-3} cm^2 s^{-1}, respectively,[17,18] at 750 °C. Notably, the D^* of PNO is an order of magnitude higher than that of $Nd_2NiO_{4+\delta}$ at 500 °C.[19]

[a] Guangzhou Power Supply Bureau, Guangdong Power Grid Co., Ltd, Guangzhou, 510620, PR China
[b] School of Materials Science and Engineering, State Key Laboratory of Material Processing and Die & Mould Technology, Huazhong University of Science & Technology, Wuhan, Hubei 430074, PR China
[c] School of Materials Science and Physics, China University of Mining and Technology, Xuzhou 221116, PR China. E-mail: yunfengup@cumt.edu.cn

† Electronic supplementary information (ESI) available. See DOI: https://doi.org/10.1039/d4tc03740e

However, PNO is less thermally stable, prone to decomposition into heterogeneous phases such as $Pr_4Ni_3O_{10}$ and Pr_6O_{11} at elevated temperatures, and has a lower electronic conductivity.[20,21] In contrast, $La_2NiO_{4+\delta}$ offers better thermal stability within the $Ln_2NiO_{4+\delta}$ family, although its electrochemical activity remains suboptimal.[22] Substitution at the B-site of PNO with transition metal elements such as Cu can lower the phase formation temperature while improving the electronic conductivity and oxygen permeability of the material.[23] Among these, $Pr_2Ni_{0.8}Cu_{0.2}O_{4+\delta}$ (PNC) has shown the lowest polarization impedance over different Cu^{2+} doping levels.[24,25]

In this study, we focused on PNC-based Ruddlesden–Popper perovskite materials and synthesized $Pr_2Ni_{0.8}Cu_{0.2}O_{4+\delta}$ (PNC), $Pr_{1.5}La_{0.5}Ni_{0.8}Cu_{0.2}O_{4+\delta}$ ($PL_{0.5}NC$), and $Pr_{1.0}La_{1.0}Ni_{0.8}Cu_{0.2}O_{4+\delta}$ (PLNC) by A-site doping with 25% and 50% La^{3+}, respectively. The synthesis was carried out by the sol–gel method. The influence of La^{3+} doping on the material properties was systematically investigated by phase analysis and physical and chemical characterization. Subsequently, the electrochemical performances of half-cell and full cells based on these materials were evaluated, allowing us to assess the impact of La^{3+} doping on the oxygen electrode performance.

2. Experimental

2.1 Materials synthesis

The materials PNC ($Pr_2Ni_{0.8}Cu_{0.2}O_{4+\delta}$), $PL_{0.5}NC$ ($Pr_{1.5}La_{0.5}Ni_{0.8}Cu_{0.2}O_{4+\delta}$), PLNC ($Pr_{1.0}La_{1.0}Ni_{0.8}Cu_{0.2}O_{4+\delta}$), and LDC ($Ce_{0.6}La_{0.4}O_{1.8}$) materials were synthesized by the sol–gel method. Taking $PL_{0.5}NC$ as an example, the preparation involved dissolving stoichiometric amounts of $Pr(NO_3)_3{\cdot}6H_2O$, $La(NO_3)_3{\cdot}6H_2O$, $Ni(NO_3)_2{\cdot}6H_2O$, and $Cu(NO_3)_2{\cdot}3H_2O$ in deionized water to form a homogeneous nitrate solution. Citric acid (CA) monohydrate and ethylenediaminetetraacetic acid (EDTA) were added as complexing agents in a molar ratio of 1 : 1 : 1.5 for metal ions, EDTA, and CA. The solution was stirred thoroughly and the pH was adjusted to 7–8 with ammonia to ensure complete dissolution. The mixture was stirred continuously at 80 °C for about 10 h until a homogeneous gel was formed. This gel was dried at 240 °C for 10 h to obtain a fluffy carbonaceous precursor, which was then ground to a fine powder and calcined at 950 °C for 3 h to obtain the RP-structured $PL_{0.5}NC$.

2.2 Cell preparation

YSZ electrolyte sheet prepared by the casting method was used as a half-cell support. To prevent unwanted chemical reactions between the electrode and the YSZ, a GDC barrier layer was screen printed on the YSZ surface. PNC, $PL_{0.5}NC$, PLNC with a solids content of 60 wt% were then prepared. These pastes were screen-printed symmetrically onto the GDC|YSZ|GDC structure, with an area of approximately 0.5 cm^2 at the central position of the barrier layer on both sides. The half-cells were then obtained by sintering at 950 °C for 2 h. For the full cell, $La_{0.8}Sr_{0.2}Ga_{0.8}Mg_{0.2}O_{3-\delta}$ (LSGM) was used as the electrolyte support. Rectangular ($24 \times 6 \times 2.5$ mm^3) dense bars of PNC, PL0.5NC, and PLNC powders were prepared by uniaxial pressing (15 MPa for 1 min) of 1.0–1.5 g of the corresponding materials in a rectangular mold, followed by sintering at 1250 °C in air for 5 h. The LSGM powder was homogenized by high-energy ball milling at 250 rpm for 24 h, then pressed into a cylindrical mold at 10 MPa pressure for 2 min and sintered at 1450 °C for 10 h to produce dense LSGM electrolyte sheets (thickness ~240 μm). The electrode paste was screen printed onto one side of the LSGM sheet as an oxygen electrode, while the opposite side was used as a fuel electrode with Ni-GDC, with the LDC acting as a barrier layer to prevent reactions between Ni and the LSGM electrolyte. Pt paste was used as the current collector for all electrodes.

2.3 Cell test and characterization

The samples were characterized by X-ray diffraction (XRD) using a PANalytical Empyrean diffractometer (Netherlands) with a 2θ range of 20° to 80° and a scan rate of 5° per min. XRD data were refined using GSAS software for peak position correction, data fitting, and phase analysis. Microscopic morphology and elemental distribution were examined using a GeminiSEM 300 field emission scanning electron microscope (FSEM). Thermal expansion in air was measured using a Netzsch DIL 402C dilatometer, heated from room temperature to 900 °C at 10 °C per min. Electrical conductivity was assessed by the standard four-probe method in air, and the response to changes in oxygen concentration was evaluated by electrical conductivity relaxation (ECR) tests. Thermogravimetric analysis (TGA) was performed using a Netzsch STA 449F3A in nitrogen, heating from 50 °C to 800 °C at 5 °C min^{-1}, to study weight loss patterns and oxygen vacancy evolution at elevated temperatures. Oxygen adsorption capacity was characterized by temperature-programmed desorption (TPD) using a Hiden DECRA 5080B instrument. Oxygen vacancy peak intensities were measured at room temperature using a Bruker A300 electron paramagnetic resonance (EPR) spectrometer. Electrochemical impedance spectroscopy (EIS) tests were performed on half-cells and full-cells with an applied perturbation amplitude of 10 mV, over a frequency range of 10^6 Hz to 10^{-1} Hz. Voltage sweeps were conducted from 1.2 V to 0 V in SOFC mode at a scan rate of 10 mV s^{-1}.

3. Results and discussion

3.1 Phase and composition analysis

Fig. 1(a) shows the XRD patterns of $Pr_{2-x}La_xNi_{0.8}Cu_{0.2}O_{4+\delta}$ (x = 0, 0.5, 1.0) powders after sintering at 950 °C for 3 h. All samples show diffraction peaks that match the standard PDF card (#87-1680) for $Pr_2NiO_{4.2}$. Notably, the undoped PNC sample exhibits secondary peaks at 2θ = 28.2° and 47.0°, which are attributed to the formation of Pr_6O_{11} due to the thermal instability of PNC at elevated temperatures. However, these secondary peaks disappear upon partial substitution of Pr^{3+} with La^{3+}, suggesting that La^{3+} doping at the A-site improves the thermal stability of the material. To further investigate the effect of La^{3+} doping on the crystal structure, the main diffraction peaks in the 31° to 34°

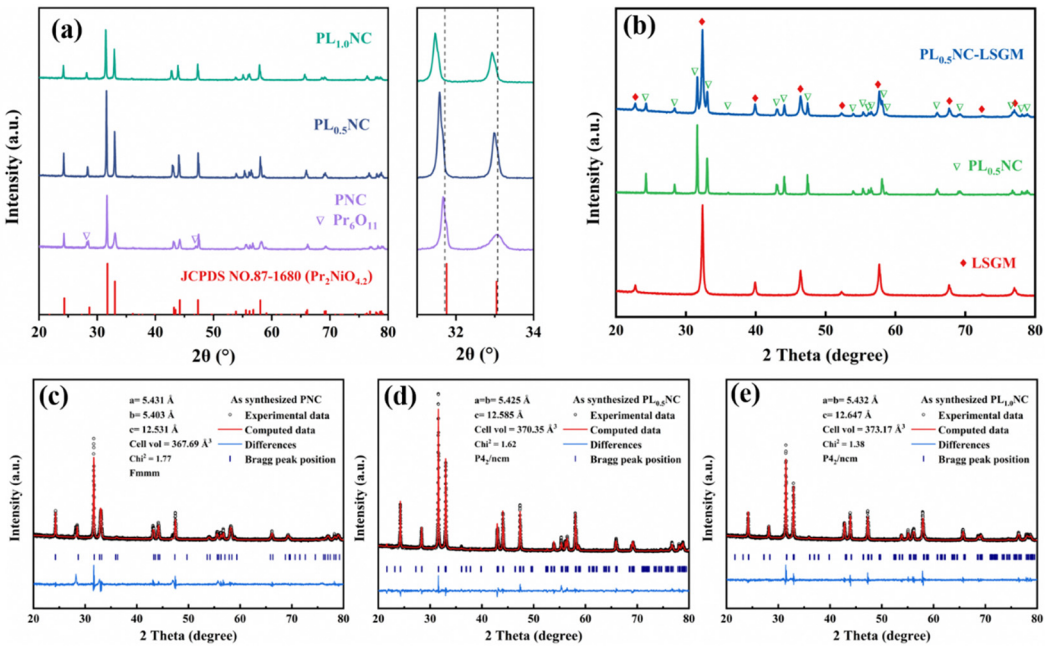

Fig. 1 XRD patterns and local magnification of $Pr_{2-x}La_xNi_{0.8}Cu_{0.2}O_{4+\delta}$ (x = 0, 0.5, 1.0) electrode powder sintered at 950 °C (a), $PL_{0.5}NC$ mixed with LSGM and calcined at 1000 °C for 10 h (b), Rietveld refinement of the XRD patterns of (c) PNC, (d) $PL_{0.5}NC$, (e) $PL_{1.0}NC$.

range were examined in detail. The results show a systematic shift of the diffraction peaks towards lower angles with increasing La^{3+} content. This shift is due to lattice expansion caused by the larger ionic radius of La^{3+} (1.061 Å) compared to Pr^{3+} (1.013 Å), leading to an overall increase in the lattice volume. Elemental diffusion and interfacial chemical reactions at the electrode/electrolyte interface are critical factors influencing ion transport. To assess the chemical compatibility of $PL_{0.5}NC$ with LSGM, a 1 : 1 mixture of $PL_{0.5}NC$ and LSGM powders was co-fired at 1000 °C for 10 h. As shown in Fig. 1(b), XRD analysis of the co-fired mixture shows no significant secondary phases, indicating that no undesirable interfacial reactions occur between the LSGM electrolyte and the $PL_{0.5}NC$ electrode within the operating temperature range of 650–800 °C. The effect of La^{3+} doping on the lattice parameters and crystal structure was further elucidated by Rietveld refinement of the XRD patterns for PNC, $PL_{0.5}NC$, and PLNC (Fig. 1(c)–(e)). The PNC sample has an orthorhombic structure (space group *Fmmm*) with lattice constants a = 5.431 Å, b = 5.403 Å, c = 12.531 Å, and a unit cell volume of 367.69 $Å^3$. In contrast, $PL_{0.5}NC$ has lattice constants $a = b$ = 5.425 Å, c = 12.585 Å, and a unit cell volume of 370.35 $Å^3$. For PLNC, the lattice constants are $a = b$ = 5.432 Å, c = 12.647 Å (Table S1, ESI†), with a corresponding unit cell volume of 373.17 $Å^3$. The increase in lattice constants and unit cell volume with higher La^{3+} doping levels is consistent with lattice expansion due to the larger ionic radius of La^{3+}. In addition, the crystal structure transitions from an orthorhombic (space group *Fmmm*) to a tetragonal (space group *P*42/*ncm*) system upon La^{3+} doping. This transformation is mainly driven by the expansion along the *c*-axis, induced by the larger La^{3+} occupying the A–O rock salt layer in the structure.[26,27] The Rietveld refinement results, with Chi^2 values below 2 for all samples, confirm the high accuracy of these structural analyses.

3.2 Physical and chemical properties

The thermal expansion coefficients (TECs) of PNC, $PL_{0.5}NC$, and PLNC were measured, as shown in Fig. 2(a). Over the temperature range of 50 to 800 °C, the average TECs were 13.55 × 10^{-6} K^{-1}, 14.44 × 10^{-6} K^{-1}, and 13.89 × 10^{-6} K^{-1}, respectively, with the materials exhibiting linear expansion with temperature. The increase in TEC with La^{3+} doping at the A-site is primarily attributed to the inverse relationship between the thermal expansion coefficient and lattice energy, which is determined by the ionic bond length; a longer bond length results in a lower bond energy.[28] As the La–O bond length is greater than that of the Pr–O bond, La^{3+} doping reduces the lattice energy, thereby increasing the TEC. However, at higher levels of La^{3+} doping, the TEC decreases slightly due to an increase in oxygen vacancies, the introduction of additional oxygen vacancies creates lattice distortions in the R–P structure, resulting in shorter metal–oxygen bond lengths compared to undoped $PrNiO_{4+\delta}$. This increase in lattice energy may cause the reduction in TEC in PLNC. For SOFC applications, it is crucial that the TECs of the electrode and electrolyte materials are closely matched to prevent mechanical problems such as electrode detachment, interfacial cracking, and delamination during high temperature operation. In this study, YSZ was used as the electrolyte for half-cells and LSGM for full-cells. The TEC of LSGM was found to be approximately 12.13 × 10^{-6} K^{-1} in the 50–800 °C range, as shown in Fig. 2(b). Table S2 (ESI†) shows a comparison of the TECs for common electrolyte materials such as YSZ,[29] GDC[30] and SDC.[31] The results indicate that $Pr_2Ni_{0.8}Cu_{0.2}O_{4+\delta}$-based Ruddlesden–Popper

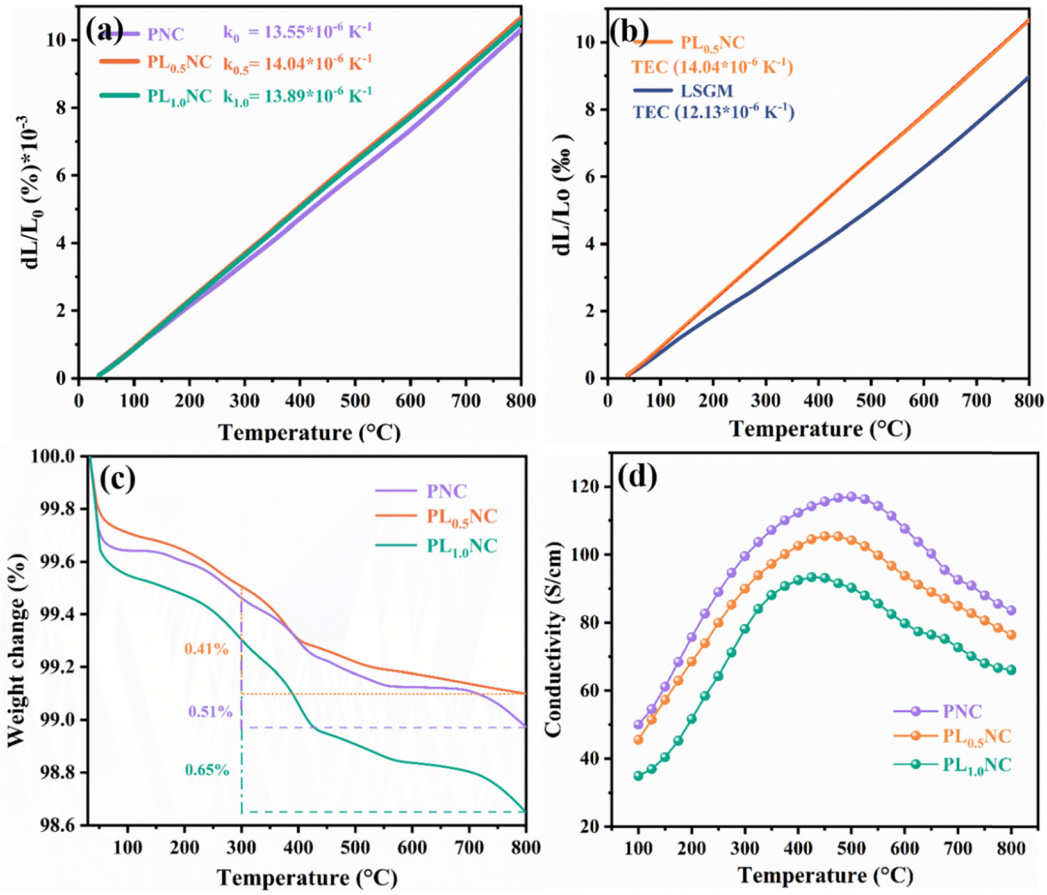

Fig. 2 Thermal expansion coefficient of (a) PNC, $PL_{0.5}NC$ and PLNC (b) $PL_{0.5}NC$ and LSGM, TG curves (c) and conductivity (d) of PNC, $PL_{0.5}NC$ and PLNC.

(R–P) perovskites have TECs that are well matched with those of commonly used electrolyte materials in SOFC. Thermogravimetric analysis (TGA) of PNC, $PL_{0.5}NC$, and PLNC in a nitrogen atmosphere, conducted between 30 °C and 800 °C, is shown in Fig. 2(c). All samples show varying degrees of weight loss with increasing temperature. The weight loss observed at lower temperatures (~300 °C) is mainly due to the volatilization and desorption of impurities such as H_2O, O_2, and CO_2 adsorbed on the sample surface. In contrast, the weight loss at higher temperatures (300–800 °C) is mainly due to the release of lattice oxygen and the formation of oxygen vacancies.[32,33] The respective weight losses for PNC, $PL_{0.5}NC$, and PLNC in the 300–800 °C range were 0.51%, 0.41%, and 0.65%. While low levels of La^{3+} doping had little effect on weight loss, a doping level of 50% resulted in a 0.14% increase in high temperature weight loss for PLNC compared to undoped PNC, suggesting that higher La^{3+} doping enhances lattice oxygen release and oxygen vacancy formation at elevated temperatures. However, the total weight loss of all samples from room temperature to 800 °C remained below 3%, indicating good thermal stability of $Pr_2Ni_{0.8}Cu_{0.2}O_{4+\delta}$-based R–P perovskites, which is beneficial for maintaining electrode material stability during device operation and high temperature testing. Conductivity measurements of PNC, $PL_{0.5}NC$, and PLNC in air, shown in Fig. 2(d), show an initial

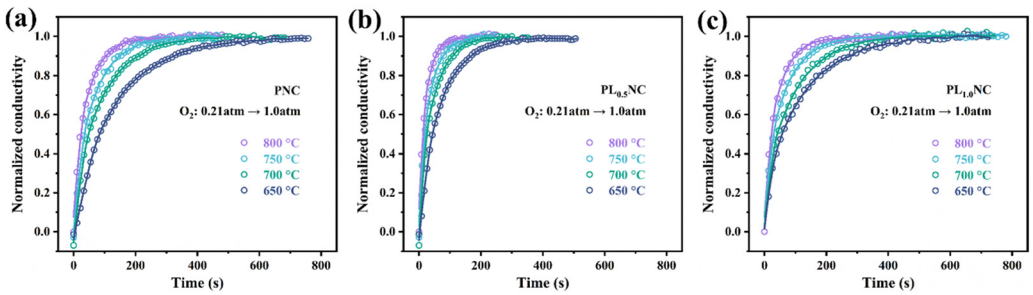

Fig. 3 ECR curves of (a) PNC (b) $PL_{0.5}NC$ (c) PLNC.

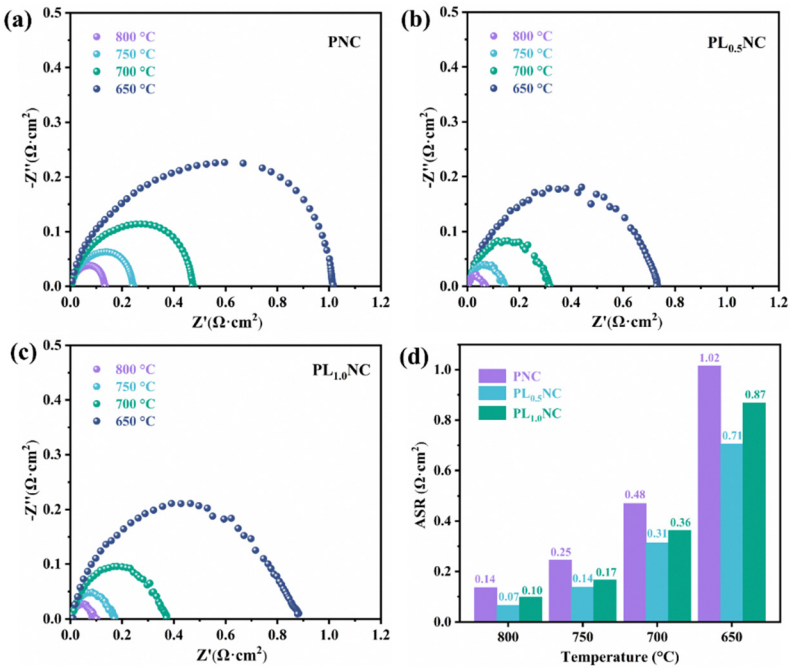

Fig. 4 Comparation of the EIS of PNC (a), $PL_{0.5}NC$ (b) and PLNC (c) electrode and histogram (d) in half-cell mode.

increase followed by a decrease in conductivity with increasing temperature in the 100–800 °C range. Initially, the materials exhibit semiconducting behavior, with thermally activated carriers (electrons and holes) contributing to the increased conductivity.[34] As the temperature continues to rise, the materials transition to metallic behavior, but continued heating reduces lattice oxygen and increases oxygen vacancies, leading to a decrease in carrier concentration and conductivity.[35] This decrease in conductivity at higher temperatures correlates with the increased weight loss observed in Fig. 2(c), indicating a significant effect of oxygen vacancy formation on conductivity. The peak conductivity for PNC, $PL_{0.5}NC$, and PLNC occurs at approximately 450 °C, with peak values of 117.2, 105.7, and 93.7 S cm^{-1}, respectively. The decrease in conductivity with increasing La^{3+} doping is mainly due to the expansion of the lattice parameters a and b, which lengthen the Ni(Cu)–O bond. This increased bond length reduces the carrier transport rate and the overall conductivity of the material.

To further elucidate the effect of La^{3+} doping on the oxygen exchange capacity, conductivity relaxation (ECR) tests were conducted. Fig. 3(a)–(c) shows the normalized conductivity curves for PNC, $PL_{0.5}NC$, and PLNC. As the oxygen electrode facilitates ORR in SOFC, the ECR test assesses the material's response to changes in oxygen partial pressure. A shorter equilibrium time indicates increased sensitivity to oxygen partial pressure, reflecting improved oxygen surface exchange and bulk diffusion capabilities. Table S3 (ESI†) summarizes the equilibrium times required at different temperatures for PNC, $PL_{0.5}NC$, and PLNC. The equilibrium time decreases with increasing temperature, consistent with the improved catalytic activity of the electrode materials at elevated temperatures. After La^{3+} doping, the equilibrium times for PL0.5NC were significantly reduced. The oxygen surface exchange coefficients (K_{chem}) and bulk diffusion coefficients (D_{chem}) for the three sample groups were determined by fitting calculations of the ECR test data (Tables S4 and S5, ESI†). These results suggest that La^{3+} doping effectively enhances the oxygen surface exchange and bulk diffusion properties of $Pr_2Ni_{0.8}Cu_{0.2}O_{4+\delta}$-based R–P perovskites, thereby improving their sensitivity to oxygen partial pressure. In particular, $PL_{0.5}NC$ exhibits the shortest equilibrium times, highest K_{chem} and D_{chem} values, highlighting its superior oxygen transport capabilities.

3.3 Half-cell performance

To further investigated the effect of La^{3+} doping on the electrochemical performance of the electrode materials, EIS was performed on half-cells with the configuration $Pr_{2-x}La_xNi_{0.8}Cu_{0.2}O_{4+\delta}|GDC|YSZ|GDC|Pr_{2-x}La_xNi_{0.8}Cu_{0.2}O_{4+\delta}$ (x = 0, 0.5, 1.0). The results shown in Fig. 4 represent the polarization impedance (R_p) after taking into account the ohmic resistance for ease of comparison. As illustrated in Fig. 4(a), the R_p values for the PNC electrode were 0.14, 0.25, 0.48, and 1.02 Ω cm^2 at 800, 750, 700, and 650 °C, respectively. The La^{3+} doped electrodes, specifically $PL_{0.5}NC$ and PLNC, exhibited significantly lower R_p compared to PNC. In particular, $PL_{0.5}NC$ showed the most significant reduction in R_p with values of 0.07, 0.14, 0.31, and 0.71 Ω cm^2 at the corresponding temperatures (Fig. 4(b)), while PLNC showed R_p values of 0.10, 0.17, 0.36, and 0.87 Ω cm^2 (Fig. 4(c)). Fig. 4(d) highlights the comparative polarization impedance of all three electrode materials at different temperatures, showing that La^{3+} doping significantly enhances the ORR catalytic activities, with the most pronounced improvement observed at a doping level of 0.5. The Arrhenius plots and activation energies for the three materials shown in Fig. S2

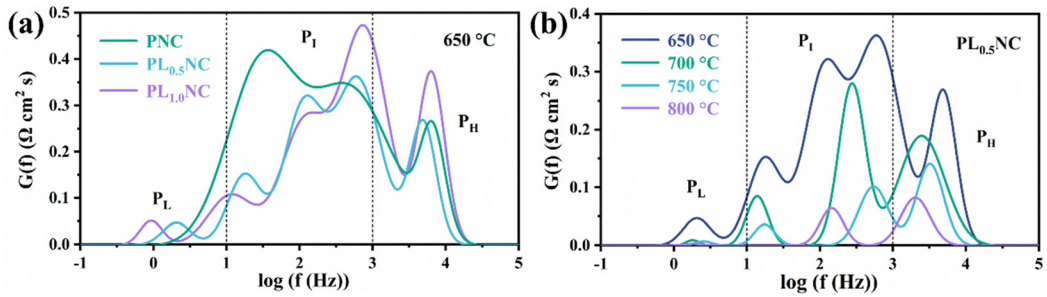

Fig. 5 DRT analysis of the impedance spectrum of half cells: (a) DRT analysis of the impedance spectrum of PNC, $PL_{0.5}NC$, PLNC at 650 °C (b) DRT analysis of the impedance spectrum of $PL_{0.5}NC$ at 650–800 °C.

(ESI†) indicate that the activation energies for PNC, $PL_{0.5}NC$, and PLNC are 136.29, 129.68, and 132.34 kJ mol^{-1}, respectively. The activation energy decreases with La^{3+} doping up to a doping level of 0.5, beyond which it increases slightly. This suggests that La^{3+} doping effectively lowers the energy barriers for ORR, with the largest reduction in activation energy occurring at a doping level of 25%. Consequently, $PL_{0.5}NC$ shows enhanced electrocatalytic activity, highlighting its potential for improved performance in fuel cells.

To further analyze the effect of La^{3+} doping on the electrode reaction processes, the impedance spectra of the half-cells were deconvoluted into three different frequency regions using the distribution of relaxation time (DRT) method: the low-frequency peak (P_L) (0.1–10 Hz), the mid-frequency peak (P_I) (10–10^3 Hz), and the high-frequency peak (P_H) (10^3–10^5 Hz), as shown in Fig. 5. Typically, the high-frequency region reflects the ion exchange process at the three-phase boundary, the mid-frequency region corresponds to charge transfer, and the low-frequency region is associated with gas adsorption and dissociation processes.[36,37] Fig. 5(a) illustrates the DRT peak fitting results for the PNC, $PL_{0.5}NC$, and PLNC half-cells at 650 °C. The total peak area in the DRT analysis decreases with increasing La^{3+} doping and then increases again, with $PL_{0.5}NC$ exhibiting the smallest peak area, consistent with the EIS results shown in Fig. 4. It is evident that La^{3+} doping has minimal effect on the peak position, shape, and width in the high-frequency region.

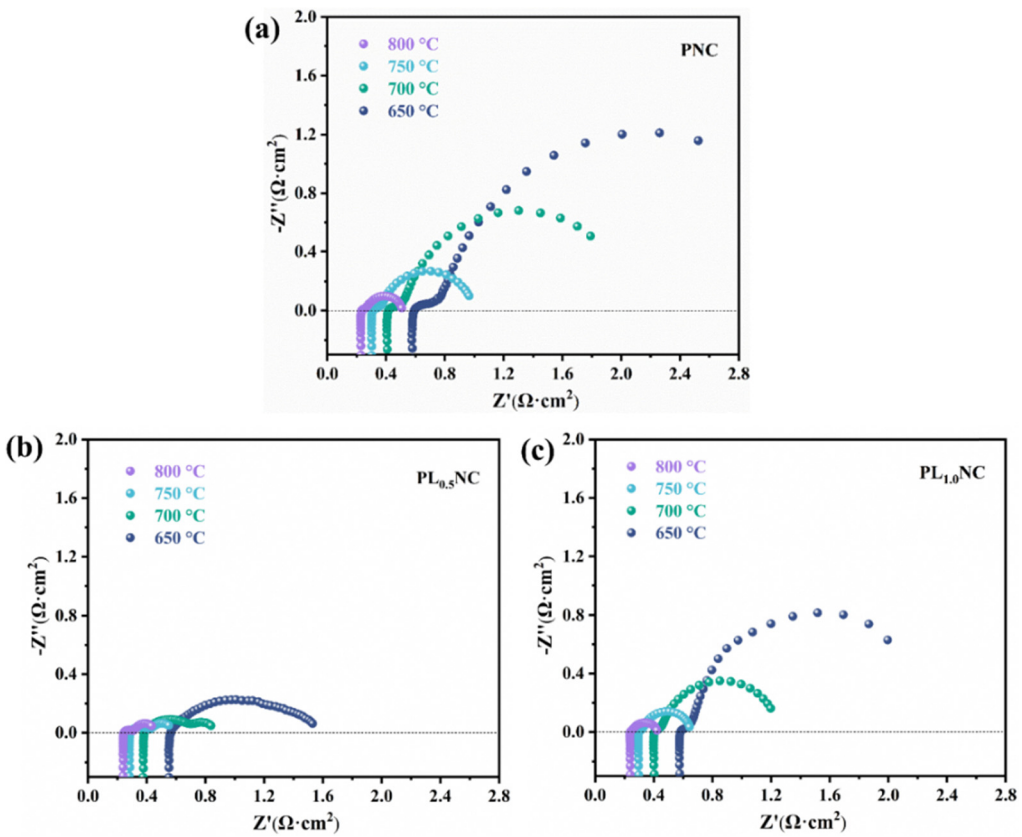

Fig. 6 EIS curves of different oxygen electrodes $Pr_{2-x}La_xNi_{0.8}Cu_{0.2}O_{4+\delta}$ (x = 0, 0.5, 1.0) single cells (a) PNC (b) $PL_{0.5}NC$ (c) PLNC.

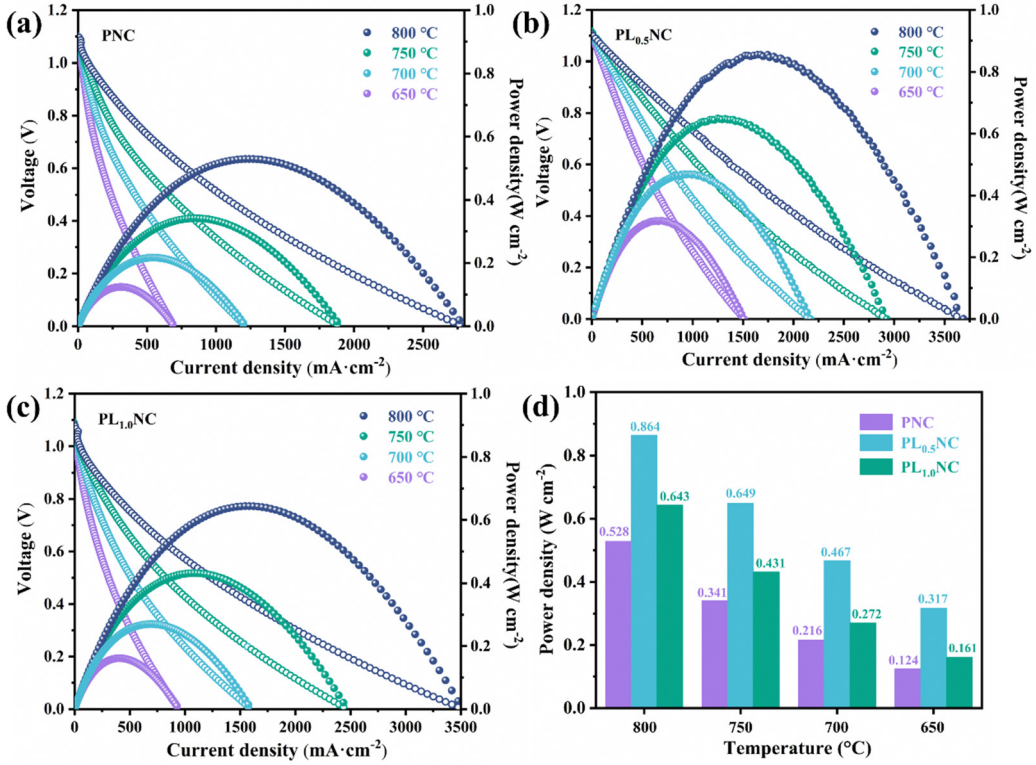

Fig. 7 *I–V–P* curves of different oxygen electrode $Pr_{2-x}La_xNi_{0.8}Cu_{0.2}O_{4+\delta}$ (x = 0, 0.5, 1.0) single cells in SOFC (a) PNC (b) $PL_{0.5}NC$ (c) PLNC, and (d) comparison of peak power density at 650–800 °C.

However, it significantly affects the low and mid frequency regions by shifting the peak positions to lower frequencies and reducing the peak areas. This suggests that La^{3+} doping mainly enhances the oxygen diffusion process on the electrode surface and the charge transfer process in the electrode response. Fig. 5(b) shows the DRT analysis results of the impedance spectrum of $PL_{0.5}NC$ half-cell at different temperatures. The total peak area progressively decreases with increasing temperature, indicating the positive effect of elevated temperatures on the electrode reaction kinetics. In contrast to Fig. 5(a), temperature changes significantly affect the peak positions, numbers, and areas across all frequency bands. At 800 °C, no distinct low-frequency peaks are observed due to the forward shift and reduction in peak area, leaving only two prominent peaks in the mid and high-frequency regions. This highlights the accelerating effect of high temperature on the electrode reaction processes and kinetics.

3.4 Full cell performance

A full cell with the structure NiO-GDC|LDC|LSGM| $Pr_{2-x}La_x$-$Ni_{0.8}Cu_{0.2}O_{4+\delta}$ (x = 0, 0.5, 1.0) was tested in SOFC mode, with the fuel electrode was supplied with humidified hydrogen (3% H_2O) and the oxygen electrode was exposed to air. EIS and current–voltage–power (*I–V–P*) characteristic measurements were carried out. The EIS curves obtained at 650–800 °C for cells using PNC, $PL_{0.5}NC$, and PLNC as oxygen electrodes are shown in Fig. 6. The total ohmic resistance (R_Ω), which is mainly determined by the ionic conduction in the electrolyte and the contact resistance between the cell components, and the R_p, which reflects the electrode reaction kinetics, were quantified. Table S6 (ESI†) summarizes the R_Ω and R_p values at different temperatures for the full cells. Both R_Ω and R_p decrease with increasing temperature due to enhanced ion and electron transport within the electrolyte and electrodes. At 650, 700, 750, and 800 °C, the R_Ω values for the PNC full cells were 0.591, 0.415, 0.310, and 0.234 Ω cm^2, respectively. For $PL_{0.5}NC$, these values were 0.564, 0.385, 0.288, and 0.245 Ω cm^2, while PLNC had R_Ω values of 0.587, 0.405, 0.297, and 0.240 Ω cm^2. The R_Ω values suggest a trend of initial decrease followed by a slight increase with higher La^{3+} doping. As the electrolyte primarily determines the R_Ω in these cells, the R_Ω shows limited variation. The R_p values for the PNC full cell were 1.933, 1.375, 0.655, and 0.272 Ω cm^2 at 650, 700, 750, and 800 °C, respectively. For $PL_{0.5}NC$, the R_p values were significantly lower at 0.965, 0.452, 0.263, and 0.189 Ω cm^2, and for PLNC, they were 1.414, 0.791, 0.345, and 0.218 Ω cm^2. The results indicate that La^{3+} doping significantly reduces the R_p, with the most significant reduction observed at a doping level of 25%. This suggests that $PL_{0.5}NC$ has superior electrocatalytic activity.

Fig. 7(a)–(c) shows the *I–V–P* curves for PNC, $PL_{0.5}NC$, and PLNC full cells measured at 650–800 °C. The open circuit voltages (OCVs) for all cells are around 1.1 V, with a slight decrease observed with increasing temperature, indicating that the cells maintain good air tightness and have dense electrolytes. Fig. 7(d) compares the peak power densities (PPD) of the three full cells at different temperatures. The PPD values follow

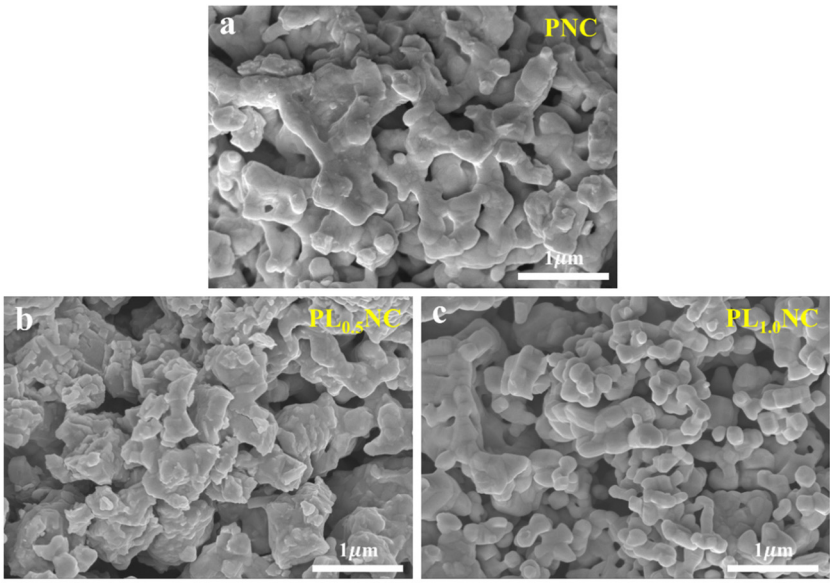

Fig. 8 SEM cross-section of (a) PNC (b) $PL_{0.5}NC$ (c) PLNC electrodes after performance test.

the trend $PL_{0.5}NC$ > PLNC > PNC, demonstrating that La^{3+} doping effectively enhances cell output performance. At 650, 700, 750, and 800 °C, the PPDs of the PNC full cell were 0.124, 0.216, 0.341, and 0.528 W cm^{-2}, respectively. In contrast, the $PL_{0.5}NC$ full cell achieved PPDs of 0.317, 0.467, 0.649, and 0.864 W cm^{-2}, while the PLNC cell exhibited PPDs of 0.161, 0.272, 0.431, and 0.643 W cm^{-2} at the corresponding temperatures. Compared to PNC, the $PL_{0.5}NC$ full cell shows a remarkable improvement in PPD of approximately 156%, 116%, 90% and 64% respectively at these temperatures. These results suggest that La^{3+} doping significantly improves cell performance, with the optimal doping level being 0.5 for the $PL_{0.5}NC$ oxygen electrode, which exhibits the highest electrocatalytic activity. Coupled with impedance spectral DRT analysis, the performance enhancement by La^{3+} doping is likely due to the promotion of oxygen surface diffusion and charge transfer processes in the electrode reaction.

To further investigated the effect of La^{3+} doping on the electrode morphology, the microstructures of PNC, $PL_{0.5}NC$, and PLNC oxygen electrodes are shown in Fig. 8(a)–(c). All three electrodes exhibit an optimal pore distribution, which facilitates oxygen adsorption and diffusion on the electrode surface, thus providing more active sites for electrochemical reactions. However, the electrode morphology changes significantly with different La^{3+} doping levels. In particular, the surface of $PL_{0.5}NC$ becomes rougher, while the particle size of PLNC decreases. Integrating these observations with the results of the half-cell and full-cell performance tests, $PL_{0.5}NC$ shows superior electrocatalytic activity compared to PNC and PLNC. This enhancement can be attributed to its relatively rough microstructure. The rough, continuous skeleton of $PL_{0.5}NC$ is likely to increase the specific surface area of the electrode, providing more active reaction sites and extending the three-phase boundary, thus accelerating the electrode reaction process.

4. Conclusion

Three materials—PNC, $PL_{0.5}NC$, and PLNC—with different levels of La^{3+} doping was successfully synthesized by the sol–gel method. The results reveal that increasing La^{3+} doping leads to a gradual decrease in electrical conductivity, with peak values of 117.2, 105.7, and 93.7 S cm^{-1} for PNC, $PL_{0.5}NC$, and PLNC, respectively. Among these, $PL_{0.5}NC$ exhibits the fastest conductivity relaxation, indicating enhanced oxygen surface exchange and bulk diffusion capabilities. La^{3+} doping effectively lowers the energy barrier for electrode reactions, as evidenced by the comparison of R_p and activation energy, following the trend: $PL_{0.5}NC$ < PLNC < PNC. The enhancement is primarily attributed to improved oxygen surface exchange and charge transfer processes. The $PL_{0.5}NC$-based cell demonstrated superior electrochemical performance, with a R_p as low as 0.245 Ω cm^2 at 800 °C and PPD of 0.864 W cm^{-2}, a 64% improvement over PNC. In conclusion, La^{3+} doping significantly enhances the catalytic activity of PNC-based electrodes, with $PL_{0.5}NC$ emerging as a promising candidate for high-performance SOFC oxygen electrodes due to its excellent physicochemical and electrochemical properties.

Author contributions

Zihao Liao: investigation, methodology, writing – original draft. Yiping Yang: data curation, formal analysis, investigation, methodology. Dingrong Ou: methodology, data curation. Yuan Tang: methodology, funding acquisition. Bo Wang: methodology, funding acquisition. Binbin He: methodology, project administration, funding acquisition. Yu Zeng: investigation, methodology. Yunfeng Tian: supervision, conceptualization writing – review & editing. Bo Chi: methodology, funding acquisition, project administration.

Data availability

The data supporting this article have been included as part of the ESI.†

Conflicts of interest

The authors declare no conflict of interest.

Acknowledgements

We acknowledge the financial support from the National Key R&D Program of China (2022YFB4002205), Southern Power Grid Corporation Science and Technology Project Funding (030100KC23020007), National Natural Science Foundation of China (52172199, 52302334), Jiangsu Province (BZ2022027, BE2023092). Changzhou City (CZ20230010). The project was also supported by the State Key Laboratory of Materials Processing and Die & Mould Technology, Huazhong University of Science and Technology (P2023-025).

References

1 S. He, Y. Zou, K. Chen and S. P. Jiang, *Interdiscip. Mater.*, 2023, **2**, 111–136.
2 M.-Y. Zhang, Y.-F. Tian, L. Zou, J. Pu and B. Chi, *Rare Met.*, 2024, 1–11.
3 H. Su, D. Wu, C. Li, C. Li and C. Zhang, *Prog. Nat. Sci.: Mater. Int.*, 2023, **33**(3), 309–319.
4 W. Li, J. Sunarso, Y. Yang, Y. Chen, C. Ge, W. Wang, Y. Guo, R. Ran and W. Zhou, *Energy Rev.*, 2024, 100085.
5 W. Wang, Y. Huang, S. Jung, J. M. Vohs and R. J. Gorte, *J. Electrochem. Soc.*, 2006, **153**, A2066.
6 Y. Liu, Y. Tian, W. Wang, Y. Li, S. Chattopadhyay, B. Chi and J. Pu, *ACS Appl. Mater. Interfaces*, 2020, **12**, 57941–57949.
7 S. P. Jiang, *Int. J. Hydrogen Energy*, 2019, **44**, 7448–7493.
8 R. Yang, Y. Tian, Y. Liu, J. Pu and B. Chi, *J. Rare Earths*, 2023, **41**, 599–604.
9 X. Xu, C. Su and Z. Shao, *Energy Fuels*, 2021, **35**, 13585–13609.
10 V. Sivtsev, E. Lapushkina, I. Kovalev, R. Guskov, M. Popov and A. Nemudry, *Green Carbon*, 2023, **1**, 154–159.
11 Y. Tian, N. Abhishek, C. Yang, R. Yang, S. Choi, B. Chi, J. Pu, Y. Ling, J. T. Irvine and G. Kim, *Matter*, 2022, **5**, 482–514.
12 Z. Li, P. Shan, W. Tang, Q. Ni, B. Qian, S. Wang, Y. Zheng, L. Ge, H. Chen and C. Zhang, *J. Alloys Compd.*, 2023, **932**, 167646.
13 D. Mishchenko, M. Arapova, Y. Bespalko, Z. Vinokurov and A. Shmakov, *J. Alloys Compd.*, 2023, **967**, 171693.
14 A. Staykov, T. Nguyen, T. Akbay and T. Ishihara, *J. Phys. Chem. C*, 2022, **126**, 7390–7399.
15 L. Navarrete, M. Fabuel, C.-Y. Yoo and J. Serra, *Int. J. Hydrogen Energy*, 2020, **45**, 15589–15599.
16 X.-D. Zhou, J. W. Templeton, Z. Nie, H. Chen, J. W. Stevenson and L. R. Pederson, *Electrochim. Acta*, 2012, **71**, 44–49.
17 N. Porotnikova, A. Khodimchuk, M. Ananyev, V. Eremin, E. Tropin, A. Farlenkov, E. Y. Pikalova and A. Fetisov, *J. Solid State Electrochem.*, 2018, **22**, 2115–2126.
18 S. Saher, J. Song, V. Vibhu, C. Nicollet, A. Flura, J.-M. Bassat and H. J. Bouwmeester, *J. Mater. Chem. A*, 2018, **6**, 8331–8339.
19 E. Boehm, J.-M. Bassat, P. Dordor, F. Mauvy, J.-C. Grenier and P. Stevens, *Solid State Ionics*, 2005, **176**, 2717–2725.
20 X. Xu, Y. Pan, Y. Zhong, R. Ran and Z. Shao, *Mater. Horiz.*, 2020, **7**, 2519–2565.
21 A. Kovalevsky, V. Kharton, A. Yaremchenko, Y. Pivak, E. Naumovich and J. Frade, *J. Eur. Ceram. Soc.*, 2007, **27**, 4269–4272.
22 A. Kovalevsky, V. Kharton, A. Yaremchenko, Y. Pivak, E. Tsipis, S. Yakovlev, A. Markov, E. Naumovich and J. Frade, *J. Electroceram.*, 2007, **18**, 205–218.
23 W. Wang, Y. Li, Y. Liu, Y. Tian, B. Ma, J. Li, J. Pu and B. Chi, *ACS Sustainable Chem. Eng.*, 2021, **9**, 10913–10919.
24 J. Hyodo, K. Tominaga, Y.-W. Ju, S. Ida and T. Ishihara, *Solid State Ionics*, 2014, **256**, 5–10.
25 A. P. Tarutin, Y. G. Lyagaeva, A. I. Vylkov, M. Y. Gorshkov, G. K. Vdovin and D. A. Medvedev, *J. Mater. Sci. Technol.*, 2021, **93**, 157–168.
26 M. Khoshkalam, Đ. Tripković, X. Tong, M. A. Faghihi-Sani, M. Chen and P. V. Hendriksen, *J. Power Sources*, 2020, **457**, 228035.
27 S. R. Maity, M. Ceretti, L. Keller, J. Schefer, T. Shang, E. Pomjakushina, M. Meven, D. Sheptyakov, A. Cervellino and W. Paulus, *Phys. Rev. Mater.*, 2019, **3**, 083604.
28 M. Hrovat, S. Bernik, J. Holc, D. Kuscer and D. Kolar, *J. Mater. Sci. Lett.*, 1997, **16**, 143–146.
29 T. Jiang, Z. Wang, B. Ren, J. Qiao, W. Sun and K. Sun, *J. Power Sources*, 2014, **247**, 858–864.
30 Y. Wang, X. Zhao, S. Lü, B. Yu, X. Meng, Y. Zhang, J. Yang, C. Fu and Y. Ji, *Ceram. Int.*, 2014, **40**, 7321–7327.
31 Q. Zhou, Y. Zhang, Y. Shen and T. He, *J. Electrochem. Soc.*, 2010, **157**, B628.
32 W. Jia, Y. Wang, J. Huang, M. Li, B. Xiang, Y. Wang, L. Wu, L. Zheng and L. Ge, *Appl. Energy*, 2024, **353**, 122096.
33 H. Gong, D. Zhou, X. Zhu, N. Wang, J. Bai, L. Hu, Y. Zhang, Y. Chen, C. Luo and W. Yan, *Int. J. Hydrogen Energy*, 2024, **50**, 1492–1502.
34 N. Dasgupta, R. Krishnamoorthy and K. T. Jacob, *Solid State Ionics*, 2002, **149**, 227–236.
35 C. Yang, Y. Tian, J. Pu and B. Chi, *ACS Sustainable Chem. Eng.*, 2022, **10**, 1047–1058.
36 M. Ghamarinia, A. Babaei, C. Zamani and H. Aslannejad, *Chem. Eng. J. Adv.*, 2023, **15**, 100503.
37 J. H. Park, C. H. Jung, K. J. Kim, D. Kim, H. R. Shin, J.-E. Hong and K. T. Lee, *ACS Appl. Mater. Interfaces*, 2021, **13**, 2496–2506.

